Lithospheric Deformation Beneath the Incipient Okavango Rift Zone Revealed by Three-Dimensional Seismic Velocity Inversion

Tuo Wang[1], Xu Wang[1], Ling Chen*[1,2], Stephen S. Gao[3], Kelly H. Liu[3], Youqiang Yu[4], and Zhichao Yu[1]

Abstract

The incipient Okavango rift zone (ORZ) in the southern end of the East African rift system is one of the youngest rift zones on Earth. Knowledge of the lithospheric structure of the ORZ is crucial to understanding the early-stage rifting processes of the rift system and even the mechanisms leading to the breakup of ancient continents. In this study, we construct a 3D lithospheric shear-wave velocity model beneath the ORZ by jointly inverting Rayleigh-wave phase velocity dispersion and receiver functions using a nonlinear Bayesian Monte Carlo algorithm. The model exhibits velocity structure from the surface to 160 km depth, and several lithospheric features associated with the continental stretching are revealed. Within the crust, low velocities are found beneath the ORZ, which could be caused by the presence of melts. We also observe four low-velocity anomalies in the upper mantle. Two of these anomalies are located at the two ends of the ORZ, probably related to decompression melting caused by the stretching of the continent. The third one is observed directly beneath the rift, which starts from ~110 km depth and extends deeper. We postulate the anomaly is attributable to the presence of a small volume of melts and/or high temperatures of the region that may be caused by hot fluids from greater depths. These three anomalies may act as melt reservoirs feeding the crust. Another low-velocity anomaly is imaged beneath the boundary between the Limpopo belt and Kaapvaal craton. Unlike the others, this feature is likely related to the compositional changes due to the reduction of Mg# in the lithospheric mantle associated the Precambrian magmatic events. As such, it may not serve as a melt reservoir in the current tectonic setting.

Cite this article as Wang, T., X. Wang, L. Chen, S. S. Gao, K. H. Liu, Y. Yu, and Z. Yu (2026). Lithospheric Deformation Beneath the Incipient Okavango Rift Zone Revealed by Three-Dimensional Seismic Velocity Inversion, *Seismol. Res. Lett.* **XX**, 1–15, doi: 10.1785/0220250269.

Supplemental Material

Introduction

Continental breakup, leading to a series of tectonic activities such as the opening of oceans, spreading of mid-ocean ridges, and subduction of oceanic plates, is an indispensable stage in the Earth's evolution. The Cenozoic East African Rift System (EARS), as the largest continental rift system, is separating the African plate into the Somalian plate to the east and the Nubian plate to the west, and thus is arguably an ideal locale to investigate continental breakup. The age span of the EARS (~45 Ma to present, Ebinger and Sleep, 1998; Boone *et al.*, 2019) provides us an ideal opportunity to better understand the process of continental extension across different rift stages. Although the mature rifts zones of the great rift system, such as the Main Ethiopian rift and Kenya rift, have been more comprehensively investigated over decades (Baker and Wohlenberg, 1971; Woldegabriel *et al.*, 1990; Mechie *et al.*, 1997; Wolfenden *et al.*, 2004; Bonini *et al.*, 2005; Dugda *et al.*, 2005; Mackenzie *et al.*, 2005; Corti, 2009; Brune *et al.*, 2017; Hubert *et al.*, 2018; Chiasera *et al.*, 2021; Ogden *et al.*, 2021; Jia *et al.*, 2023), knowledge of the early-stage rifts, such as the late Pleistocene Okavango rift zone (ORZ), still remains limited.

---

1. State Key Laboratory of Lithospheric and Environmental Coevolution, Institute of Geology and Geophysics, Chinese Academy of Sciences, Beijing, China, https://orcid.org/0000-0001-7492-8985 (TW); https://orcid.org/0000-0002-7126-4957 (XW); https://orcid.org/0000-0001-7170-5954 (LC); 2. College of Earth and Planetary Sciences, University of Chinese Academy of Sciences, Beijing, China; 3. Department of Earth Sciences and Engineering, Missouri University of Science and Technology, Rolla, Missouri, U.S.A., https://orcid.org/0000-0001-7530-7128 (SSG); https://orcid.org/0000-0001-7691-9556 (KHL); 4. State Key Laboratory of Marine Geology, Tongji University, Shanghai, China, https://orcid.org/0000-0003-2115-5055 (YY)

*Corresponding author: lchen@mail.iggcas.ac.cn

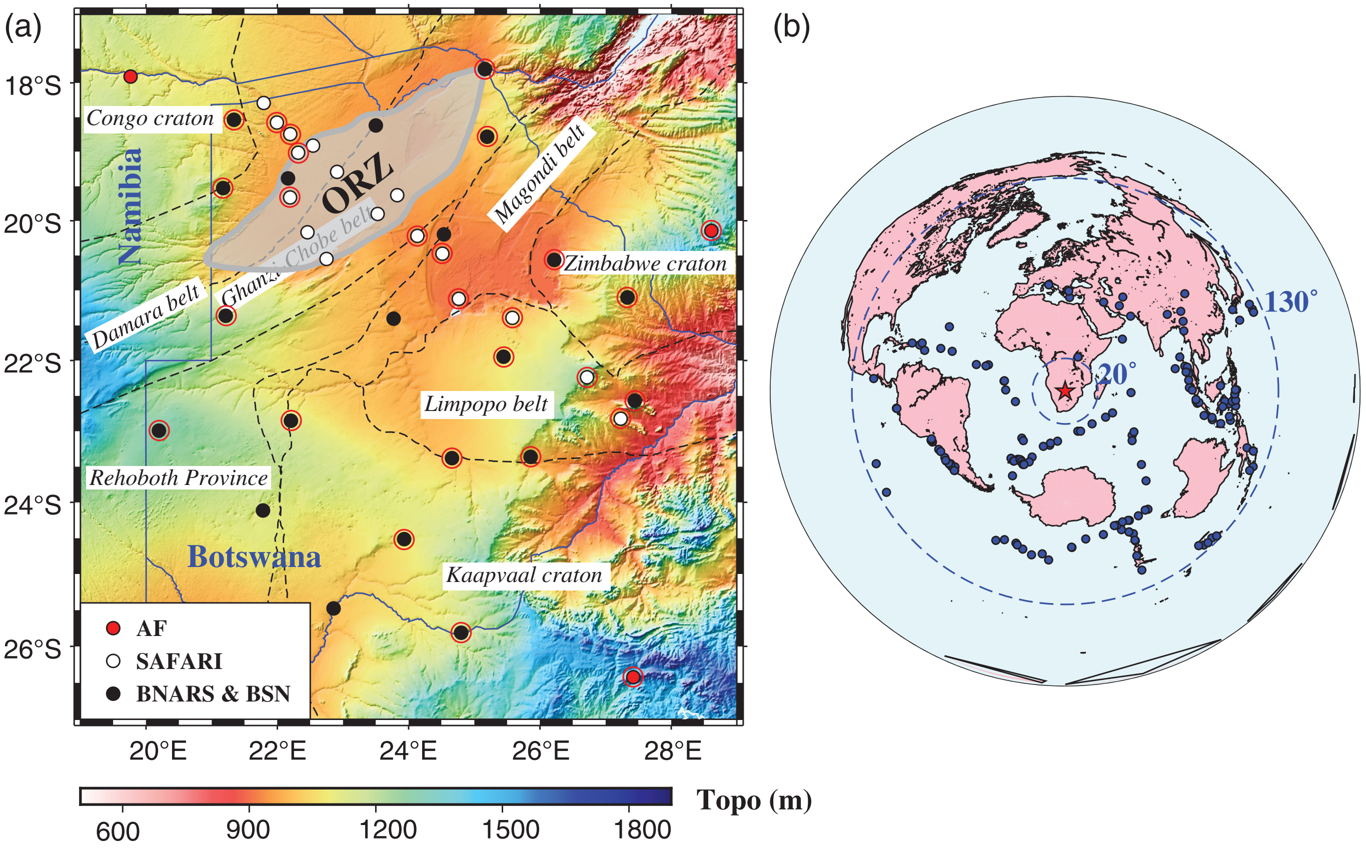

Figure 1. (a) Topographic map of the study area showing the distribution of seismic stations (filled circles). Station sites enclosed by red circles represent the ones that provide high-quality receiver functions (RFs) used for the joint inversion. The blue-solid curves represent nation boundaries, and the black dashed curves divide the major tectonic units, with the gray shade representing the Okavango rift zone (ORZ). Different experiments for the seismic stations used in this study: red: AfricaArray (AF); black: Botswana Network of Autonomously Recording Seismographys (BNARS) and Botswana Seismological Network (BSN); white: Seismic Arrays for African Rift Initiation (SAFARI). (b) Locations of the teleseismic events (167 blue dots) used in the study are plotted in an azimuthal equidistant projection map. The red pentagram represents the center of our study region.

Imagining the lithospheric structure beneath rifts allows us to better understand the processes of continental extension and breakup. However, structural features of the lithosphere of mature rifts might have been deformed or reworked by subsequent tectonic activities, hindering the understanding of the early-stage lithospheric features that are associated with the initiation of rifting. The ORZ (∼120 to 40 Ka, Reeves, 1972; Kinabo *et al.*, 2008) lying in the southern terminus of the EARS is one of the youngest continental rifts in the world, which provides an optimal opportunity to further unveil the nature of early-stage continental extension.

The nascent ORZ developed within the northeast–southwest-trending Mesoproterozoic-Early Paleozoic Damara and Ghanzi-Chobe belts (Begg *et al.*, 2009; Khoza *et al.*, 2013; Fig. 1). To the east of these belts lies another northeast–southwest-trending belt, the Paleoproterozoic Magondi belt, which marks the western margin of the Archean Zimbabwe craton (Treloar, 1988; Majaule *et al.*, 2001). The east–west-trending late Archean Limpopo belt sutures the Zimbabwe craton to the north and Kaapvaal craton to the south, forming the major portion of the composite Kalahari craton (Begg *et al.*, 2009). The southwestern part of our study region is mostly occupied by the Rehoboth Province, located along the boundary of Botswana and Namibia, which is poorly documented due to the coverage of Kalahari sands (Van Schijndel *et al.*, 2014).

Previous investigations suggest that the ORZ has a thinner crust (<40 km) compared to the surrounding regions (Leseane *et al.*, 2015; Yu, Liu, *et al.*, 2015; Fadel *et al.*, 2018; Wang *et al.*, 2025), with the thinnest crust (<30 km) in the northeastern portion of the rift (Leseane *et al.*, 2015). The higher-than-normal crustal V_P/V_S values of the ORZ (Yu, Liu, *et al.*, 2015; Fadel *et al.*, 2018; Wang *et al.*, 2025), along with the shallow Curie depth point (Leseane *et al.*, 2015), may suggest the presence of melts in the crust of the rift. A thermochemical model suggests a lithospheric thickness of ∼130 to 170 km beneath the ORZ (Afonso *et al.*, 2022), which is generally consistent with a previous tomography study (∼150 km, Yu *et al.*, 2017) and a magnetotelluric study (∼160 km, Muller *et al.*, 2009). Compared with the thicker lithosphere of the Congo craton to its northwest (~250 km thick, Khoza *et al.*, 2013; ~300 to 350 km thick, Yu *et al.*, 2017) and of the Kaapvaal and Zimbabwe cratons to its southeast (~220 to 300 km thick, James *et al.*, 2001; Muller *et al.*, 2009; Miensopust *et al.*, 2011; Yu *et al.*, 2017; Afonso *et al.*, 2022), the ORZ is characterized by an evident lithospheric thinning. An approximately −1.0% low-velocity anomaly in the upper mantle of the ORZ depicted by Yu *et al.* (2017), as also supported by other velocity models of the region (Ortiz *et al.*, 2019; Fadel *et al.*, 2020), is interpreted as the result of decompression melting associated with the lithospheric thinning (Yu *et al.*, 2017).

In this study, we attempt to enrich the knowledge of the incipient ORZ by constructing a high-resolution 3D shear velocity model through jointly inverting Rayleigh-wave phase velocity dispersion and receiver functions (RFs). Surface-wave dispersion can effectively provide velocity information at different depths but are not sensitive to the interfaces below the surface (i.e., Moho discontinuity), whereas RFs are good at recognizing these interfaces and thus improve the vertical resolution of the inverted velocity model (Julia *et al.*, 2000; Bodin *et al.*, 2012; Shen, Ritzwoller, and Schulte-Pelkum, 2013; Shen, Ritzwoller, Schulte-Pelkum, and Lin, 2013). Our model sheds new light on the features of the lithospheric structure and the potential processes of the lithospheric deformation beneath the young African rift.

Data

We use raw seismic data recorded by 41 broadband seismic stations distributed in the study region (Fig. 1). The 17 stations of the Seismic Arrays for African Rift Initiation (SAFARI; Gao *et al.*, 2012; see Data and Resources) experiment are deployed along a 756-km-long northwest–southeast-trending profile traversing the ORZ, during the period of May 2012 to June 2014 (white-solid circles in Fig. 1). The 21 stations of the Botswanan Network of Autonomously Recording Seismographs (BNARS; Utrecht University [UU Netherlands], 1983; see Data and Resources) experiment during 2013–2018 and of the Botswana Seismological Network (BSN; Botswana Geoscience Institute, 2001; see Data and Resources) experiment between 2018 and 2021 are evenly distributed across Botswana (black-solid circles in Fig. 1). In addition, there are three permanent broadband seismic stations from the AfricaArray network (AF; Penn State University, 2004; see Data and Resources), locating in the Congo, Zimbabwe, and Kaapvaal cratons, respectively (red-solid circles in Fig. 1).

Ambient seismic noise data are used to extract Rayleigh-wave phase velocity dispersion measurements at relatively short periods. Only the vertical-component waveforms are requested from the Seismological Facility for the Advancement of Geoscience (SAGE) Data Management Center (DMC), as these waveforms contain stronger Rayleigh-wave energy than the other components. For longer periods, teleseismic data are used to extract Rayleigh-wave phase velocity dispersion measurements. Three main constraints are applied for requesting teleseismic events from the SAGE-DMC (Yao *et al.*, 2005): (1) the moment magnitude (M_w) of the events should be greater than 5.0 and less than 6.8; (2) the focal depth should be less than 100 km to ensure clear signals; (3) the epicentral distance should range between 20° and 130° (the large blue dashed circles on the azimuthal equidistant projection map, Fig. 1b) to avoid near-source effects and interference from higher modes of Rayleigh wave and to depict structures in greater depth with more high-quality signal (Yao *et al.*, 2005). Under the constraints, 167 teleseismic events were used for obtaining dispersion curves (blue dots in Fig. 1b).

For RF data, approximately 990 teleseismic events are requested for the recording period from January 2006 to October 2021. A four-pole, two-pass Bessel band-pass filter (0.08–0.8 Hz) is applied on the three-component seismograms windowed to 20 s prior to and 50 s following the theoretical first *P*-wave arrival based on the IASP91 Earth model (Kennett and Engdahl, 1991). The processed seismograms are converted to radial RFs using the procedure of Ammon (1991). Detail information can be found in a recent investigation of Wang *et al.* (2025).

Methods

Surface-wave dispersion data processing

To obtain Rayleigh-wave phase velocity dispersion curves from ambient seismic noise data (3–30 s), we apply the empirical Green's function (EGF) analysis (Yao *et al.*, 2006), which consists of three main steps. First, data from each station are preprocessed by removing the instrument response, eliminating the mean and trend, applying a second-order Butterworth filter (0.025–0.5 Hz), and using one-bit temporal normalization to reduce effects on cross correlations from earthquakes and spectral whitening to suppress interferences from persistent monochromatic sources. Second, cross-correlation functions between one-day-long (86,400 s) waveforms of all station pairs are computed temporally and stacked to enhance the signal-to-noise ratio (SNR). The negative lags (i.e., "acausal" signals) of the stacked cross-correlation functions are reversed and averaged with the positive lags (i.e., "causal" signals) to reduce the deviation effects caused by the uneven distribution of the ambient noise sources (Fig. 2b,c). Third, the EGFs are obtained from the time derivatives of cross-correlation functions to enhance the higher frequencies (Sabra *et al.*, 2005a,b). A total of 820 Rayleigh-wave phase velocity dispersion curves ($n(n-1)/2$, in which n is the number of seismic stations used) with an interval of 3 s (Fig. 2d) are extracted from the same amount of EGFs using an image transformation analysis technique (Yao *et al.*, 2005). We manually select 391 reliable dispersion curves under three main constraints (Yao *et al.*, 2006; Bensen *et al.*, 2007; Wang *et al.*, 2019), which are (1) the interstation spacing should be at least three times of the wavelength (Bensen *et al.*, 2007; Yang *et al.*, 2010), (2) the SNR for each dispersion measurement should be greater than or equal to 5 (Yao *et al.*, 2006;

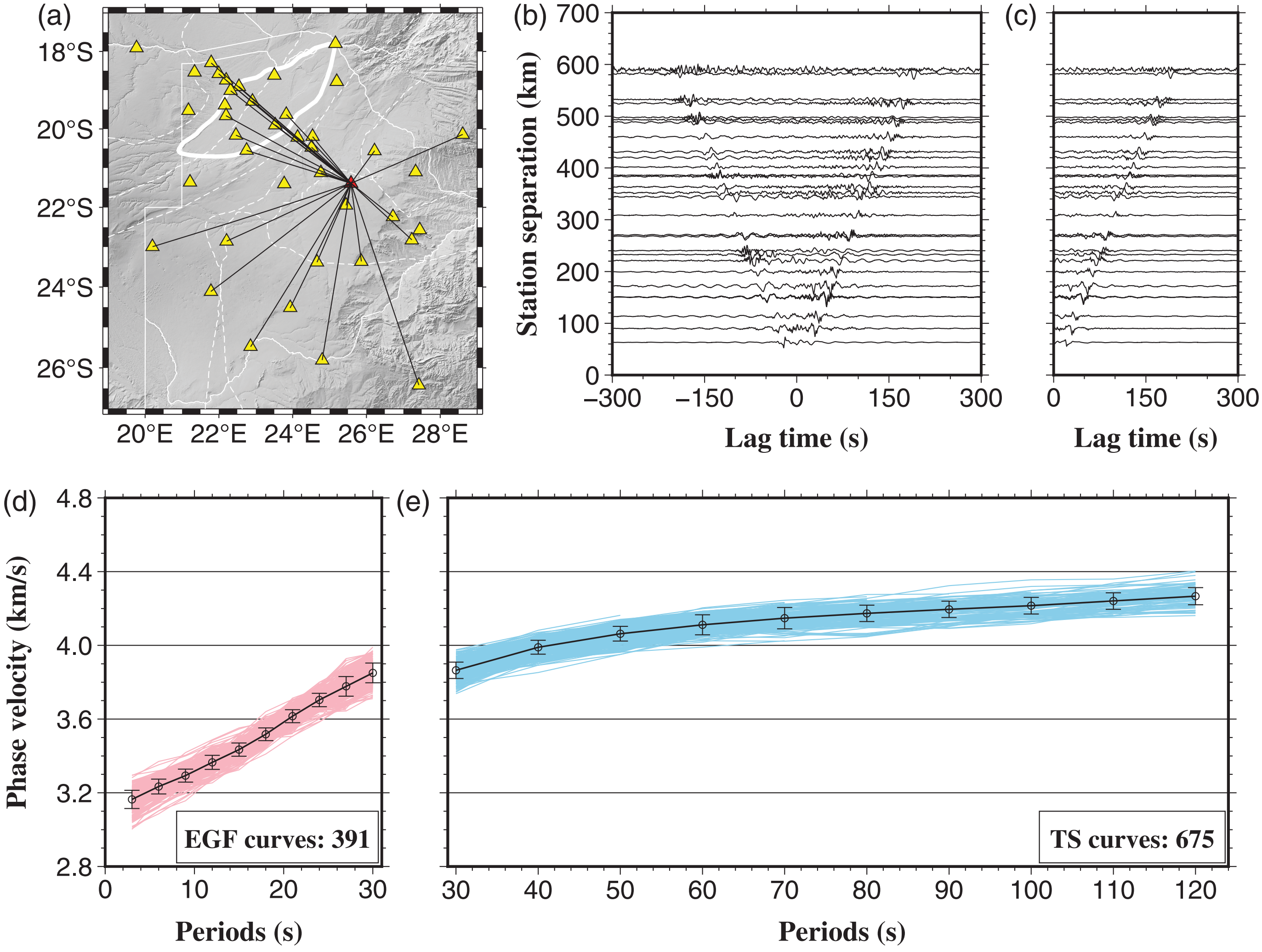

Figure 2. (a) Ray paths of cross correlation between station B02LT (red triangle) and 29 other stations (yellow triangles) of the empirical Green's function (EGF) analysis. (b) Cross-correlation functions of the 29 station pairs. (c) Cross-correlation functions after reversing the negative lags and averaging with the positive lags. (d) Manually selected Rayleigh-wave phase velocity dispersion curves using the EGF analysis. The open circles and the black curve represent the mean values of all the selected measurements at corresponding periods. (e) Similar to panel (d), but for dispersion curves from the two-station (TS) analysis.

Wang *et al.*, 2019), and (3) the selected dispersion curves should generally agree with a global model (Shapiro and Ritzwoller, 2002).

For periods from 30 to 120 s, Rayleigh-wave phase velocity dispersion curves are extracted using the teleseismic surface wave two-station (TS) analysis (Yao *et al.*, 2005). The instrument responses of each station are first removed, and the multiple filter technique is employed (Dziewonski *et al.*, 1969). The processed seismograms are then filtered with a windowed (Kaiser window) linear-phase finite impulse response band-pass filter with 0.4-s band at each period of interest. After processing the cross correlation, image transformation, and manual selection constrained by a global model (Shapiro and Ritzwoller, 2002), 675 Rayleigh-wave phase velocity dispersion curves with an interval of 10 s are obtained (Fig. 2e). Because a station pair can provide more than one dispersion curve, we have obtained ~73% more dispersion curves than the EGF analysis. The TS analysis assumes that surface waves propagate along great circle paths, which means the angle between the paths of a teleseismic event and any station pair should be less than 2° (Yao *et al.*, 2005). The selected phase velocity dispersion curves from both the EGF and TS analyses are inverted to horizontal phase velocity maps (Montagner, 1986; Yao *et al.*, 2010) at all periods with a grid dimension of 0.3° × 0.3° and a sampling of 0.1° (Fig. 3).

RF data processing

The RF data used are provided by Wang *et al.* (2025), and the procedure of data processing is briefly introduced here. Considering the presence of unconsolidated sediments within the study area (Pretorius, 1984; Ringrose *et al.*, 2005), a resonance removal filter (Yu, Song, *et al.*, 2015) is applied to suppress the reverberations on the RF time series caused by the

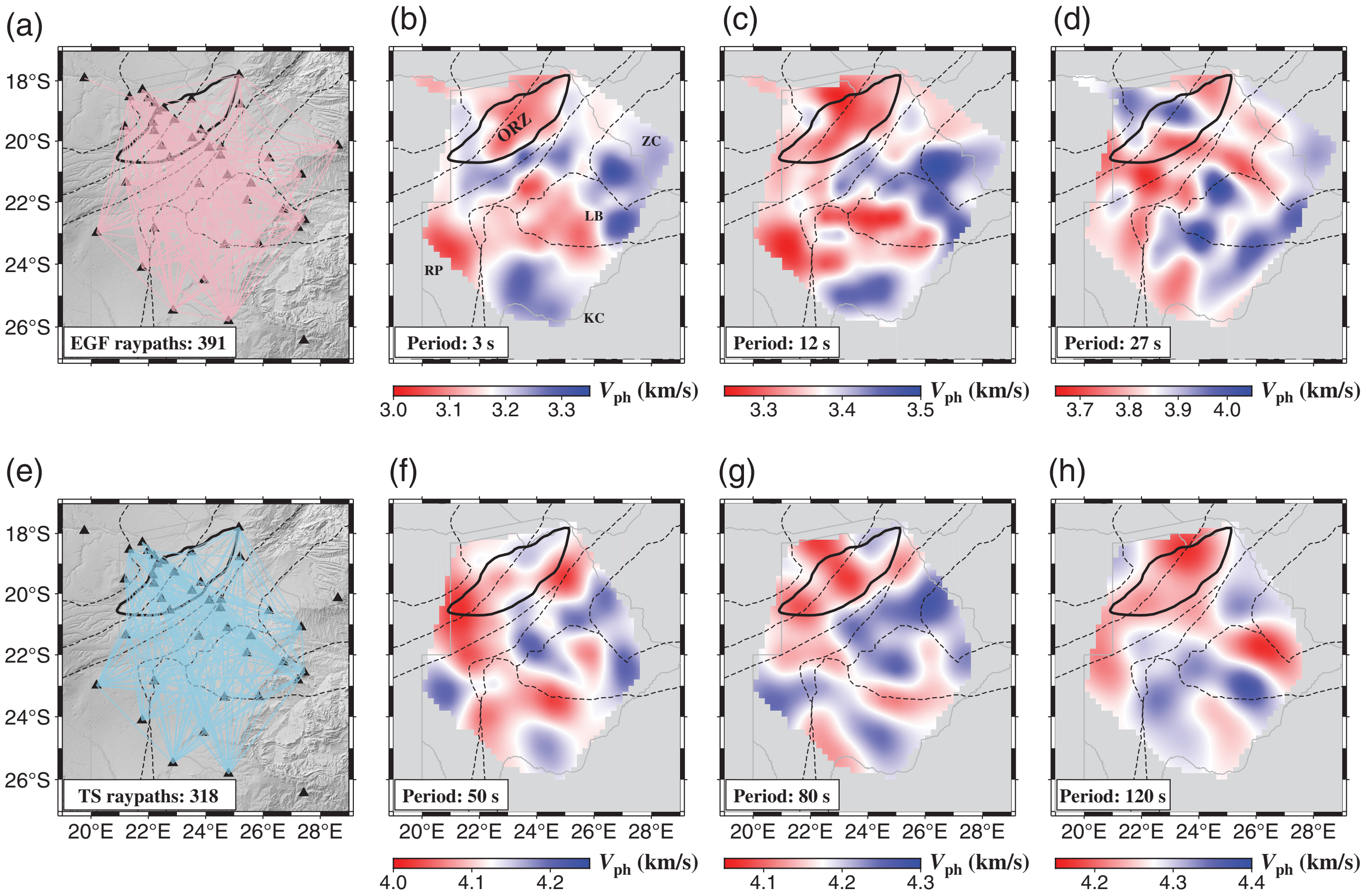

Figure 3. (a) Ray-path coverage for the EGF analysis. (b–d) Rayleigh-wave phase velocity maps at 3, 12, and 27 s obtained from the EGF analysis. (e) Ray-path coverage for the two-station (TS) analysis. (f–h) Rayleigh-wave phase velocity maps at 50, 80, and 120 s obtained from the TS analysis. KC, Kaapvaal craton; LB, Limpopo belt; ORZ, Okavango rift zone; RP, Rehoboth Province; Vph, phase velocity; and ZC, Zimbabwe craton.

sediments (Wang *et al.*, 2025), which would mask the *P-to-S* conversions from the Moho (*Pms*) and the corresponding multiples (*PPms* and *PSms*) and lead to unreliable crustal thickness (H) and V_P/V_S ratio estimates (Langston, 2011; Cunningham and Lekic, 2019). A conventional $H-\kappa$ stacking procedure (Zhu and Kanamori, 2000) is applied for RFs moveout corrections and stacking with weighting factors of 0.6, 0.3, and 0.1 for the *Pms*, *PPms*, and *PSms* phases (e.g., Nair *et al.*, 2006; Fadel *et al.*, 2018), respectively, to enhance the maximum stacking amplitude and to determine the optimal H–V_P/V_S pairs through grid searching (Fig. S1b, available in the supplemental material to this article).

Inversion for shear-wave velocities

A nonlinear Bayesian Monte Carlo algorithm is applied to invert for shear-wave velocity structures following the procedures of Shen, Ritzwoller, and Schulte-Pelkum (2013) and Shen, Ritzwoller, Schulte-Pelkum, and Lin (2013). Based on the quality of RFs, the stations are categorized into two groups. The first group consists of 27 stations (station sites enclosed by red-open circles in Fig. 1) with high-quality RF data, characterized by a clear *Pms* in the stacked RF along with clear estimates of the optimal H and V_P/V_S ratio. We jointly invert surface-wave dispersion curves with the stacked RFs during the inversion using a 0.3 weight for the RF data (Fig. 4a–f). Our tests show that the weighting factor of 0.3 can correctly identify the interfaces beneath the surface from RF time series while allowing a larger weighting factor to dispersion data for acquiring shear-wave velocity information (Text S1). The 27 stacked RFs used for the joint inversion are provided by Wang *et al.* (2025) and shown in Figure S1c. The second group includes stations with RFs showing ambiguous *Pms* arrivals in the RFs and/or unclear optimal H–V_P/V_S pair. For these stations, to avoid unreliable inversion results caused by the RFs, only surface-wave dispersion is used for the shear velocity inversion (Fig. 4g–j).

We parametrize our model using a three-layer initial inversion model for each station (black-solid curve in Fig. 4a). The upper layer represents low-velocity sediments. This layer is described by the thickness of the layer (i.e., Pretorius, 1984; Fadel *et al.*, 2020) and linear gradient shear velocities defined by the values at the top and bottom of the layer (Shen, Ritzwoller, Schulte-Pelkum, and Lin, 2013). The middle layer

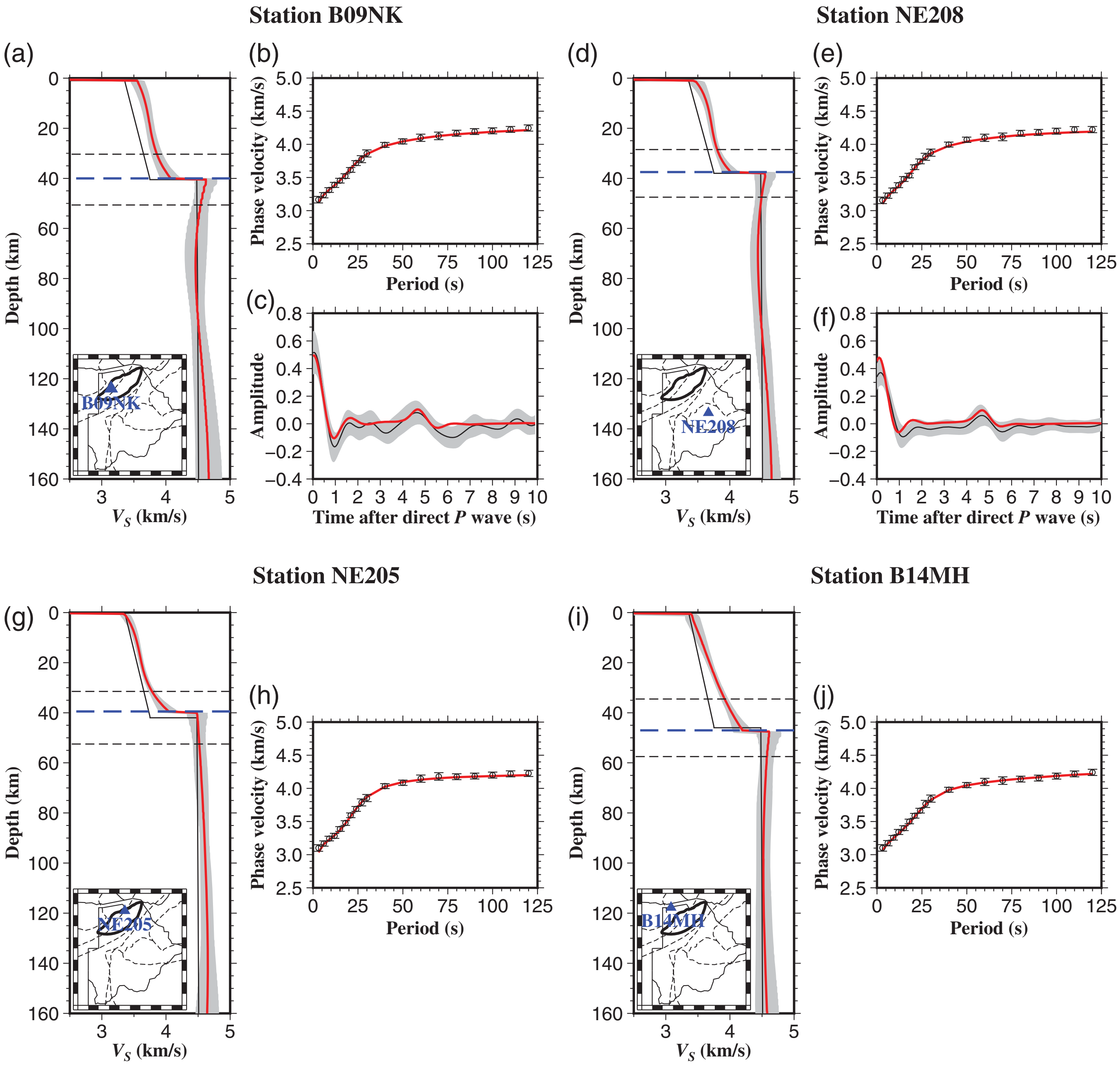

Figure 4. Examples of joint inversion results for stations (a–c) B09NK and (d–f) NE208 and surface-wave inversion results for stations (g–h) NE205 and (i–j) B14MH. (a) The black-solid curve represents the initial inversion model for station B09NK. The red curve is the inverted shear velocities, and the gray shade represents the one standard deviation (1σ) of the red curve. The horizontal blue dashed curve represents the Moho under the assumption that the Moho is a sharp velocity gradient (Shen, Ritzwoller, Schulte-Pelkum, and Lin, 2013). The two horizontal black dashed lines show the searching range, which is ± 25% perturbation of the H value for the initial model. (b) The observed phase velocities (black open circles with 1σ error bars) and predicted phase velocities (red curve) from the best fitting in panel (a). (c) The stacked RF (black curve) with the estimated 1σ uncertainty (gray shade) related to the stacking of the azimuthally independent RFs and the predicted RF (red curve) from the best fitting in panel (a). (d–f) Similar to panels (a–c), but for station NE208. (g,h) and (i,j) Similar to (a,b), but for surface-wave inversion at stations NE205 and B14MH, respectively.

---

is for the crystalline crust. The thickness of this layer is determined as the difference between the thickness of the crust (Yu, Liu, *et al.*, 2015; Fadel *et al.*, 2018; Wang *et al.*, 2025) and the corresponding sediments. Four B-spline coefficients are used to describe structures within this layer by converting them to shear velocities as a function of depth, and the initial shear velocity information for the coefficients is provided by the IASP91 velocity model (Kennett and Engdahl, 1991). The lower layer represents the lithospheric mantle. The thickness of this layer is between the bottom of the crystalline crust and 160 km depth, which is about one-third of the maximum wavelength of our surface waves, so that to invert for reliable shear velocities (Yang *et al.*, 2010). Five B-spline coefficients for shear velocities are applied in this layer with initial values from the IASP91 model. A damping is not required during the inversion since the smoothness of the model is imposed by the parametrization (Shen, Ritzwoller, Schulte-Pelkum, and Lin, 2013).

The crustal V_P/V_S values used for the initial models are mainly from our previous RF work of Wang *et al.* (2025; for 33 initial models), with 8 of them from other RF investigations (Yu, Liu, *et al.*, 2015; Fadel *et al.*, 2018). For density, following Shen, Ritzwoller, and Schulte-Pelkum (2013) and Shen, Ritzwoller, Schulte-Pelkum, and Lin (2013), we apply the scaling relation that has been influenced by Brocher (2005) and Christensen and Mooney (1995) in the upper and middle layers and by Karato (1993) in the lower layer. A physical dispersion correction (Kanamori and Anderson, 1977) with Q values from the preliminary reference Earth global model (Dziewonski and Anderson, 1981) is used. Finally, the same constraints as those of Shen, Ritzwoller, and Schulte-Pelkum (2013) and Shen, Ritzwoller, Schulte-Pelkum, and Lin (2013) are applied to determine the prior and posterior distribution (Text S2).

One limitation for the three-layer discretization is that some sublayers within the three layers could be ignored. This may not affect our inverted model because there is little evidence suggesting the existence of such sublayers in this region. Another limitation is that the algorithm is not designed to accommodate RF signals other than those related to the sediment–basement crust and Moho discontinuities to prevent increasing uncertainties and overinterpreting data (Shen, Ritzwoller, Schulte-Pelkum, and Lin, 2013). In addition, the shortest period of surface-wave dispersion measurements used for the inversion is 3 s, and thus our inverted model has limited constraints on structures shallower than ~3 km, which is about one-third of the maximum wavelength at the period of 3 s (Yang *et al.*, 2010). Given that, we do not discuss shallow structures in the study, including the layer of unconsolidated sediments.

Results

Phase velocities and resolution test

At periods of 3 and 12 s, the ORZ, Rehoboth Province, and the western portion of the Limpopo belt exhibit low phase velocities, whereas the eastern portion of the Limpopo belt and most of the Kaapvaal and Zimbabwe cratons show high phase velocities (Fig. 3b,c). At the longer periods of 50 and 80 s, one could observe low phase velocities lying in the ORZ and the surrounding belts and along the boundary of the Limpopo belt and Kaapvaal craton (Fig. 3f,g). At the longest period of 120 s, the most notable low phase velocities are found within the ORZ, whereas high phase velocities are predominantly found in the cratonic regions (Fig. 3h).

To assess the robustness of the inverted phase velocities, we apply a standard checkerboard resolution test at different periods (Fig. 5). The correlation length (L) is used to balance the smoothness of the inverted results and resolving power (Yao *et al.*, 2005, 2006). We apply different correlation lengths for different period ranges (60 km for 3–27 s and 80 km for 30–120 s) after testing (Text S3). The synthetic target model is generated with alternate red and blue 1.5° checker representing the velocities of 3.8 and 4.2 km/s, respectively. After applying the same procedures as those for real data, the recovery results indicate that our data and procedures can resolve anomalies with scales of 1.5° in the central part of the study region, where the resolution is understandably better than that near the marginal areas (Fig. 5a–f). Although anomalies with scales smaller than 1.5° could still appear, given that the inversion grid size is 0.3°, they are not well resolved and thus are not discussed.

Three-dimensional shear velocity model

Inverted shear-wave velocity curves are obtained at all the seismic stations, from either the joint inversion of Rayleigh-wave phase velocity dispersion and RFs or solely the surface-wave inversion where reliable RFs are unavailable. Each of the inverted shear velocity curves shows a sediment–basement crust discontinuity and a Moho discontinuity defined by the sharp velocity contrasts. In addition, the inverted shear velocities vary with depth with a step of 0.5 km through the sediments, crystalline crust, and the upper mantle. Figure 4a–f shows two examples of the joint inversion results at station B09NK within the ORZ and station NE208 outside the rift, whereas Figure 4g–j shows two examples of the surface-wave inversion results at station NE205 within the rift and station B14MH outside the rift, respectively.

The inverted shear velocity curves are assembled and linearly interpolated to construct a 3D shear velocity model. Patterns of the high- and low-seismic velocities from the horizontal shear velocity slices (Fig. 6) are similar to those of the phase velocity maps at corresponding periods. In the upper crust (5 km, Fig. 6a), relatively low velocities are found within the ORZ and adjacent regions, compared to the average velocity values at depth. The low velocities underneath the ORZ persist to 25 km depth but with a shrunken covering area, whereas high velocities are found in the Zimbabwe and Kaapvaal cratons (Fig. 6b). At 50 and 80 km depth, the low velocities within the ORZ vanish and split into two low-velocity anomalies at the two ends of the rift (LVA1 and LVA2 in Fig. 6c,d). Starting from 120 km depth, low velocities appear within the ORZ again (LVA3 in Fig. 6e), and another low-velocity anomaly is found beneath the boundary of the Limpopo belt and Kaapvaal craton (LVA4 in Fig. 6e). LVA3 and LVA4 persist at the depth of 160 km, whereas LVA1 and LVA2 fade away (Fig. 6f).

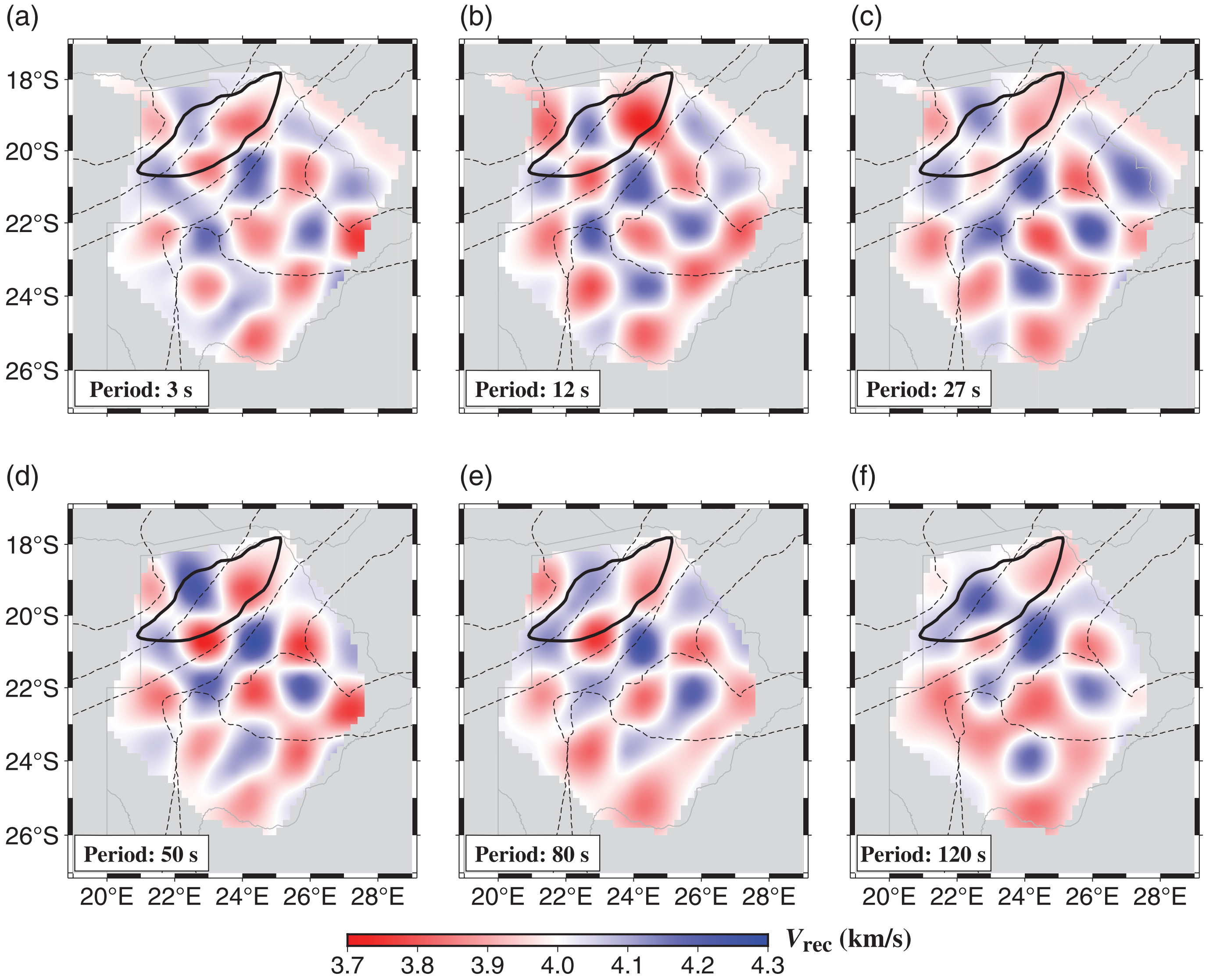

Figure 5. Standard checkerboard resolution test with grid scale of 1.5° × 1.5° at (a) 3, (b) 12, (c) 27, (d) 50, (e) 80, and (f) 120 s. The coverage for the recovery maps between 3 and 27 s is defined by the ray-path coverage for the EGF analysis (Fig. 3a), and the coverage for the recovery maps between 50 and 120 s is defined by the ray-path coverage for the TS analysis (Fig. 3e). V_{rec}, recovery velocity.

We also exhibit vertical shear velocity cross sections along two profiles (Fig. 7), with one generally being parallel to the rift axis (profile AA′ marked in Fig. 6f) and the other transecting the ORZ (profile BB′ marked in Fig. 6f). The distribution of the velocity anomalies can be better observed from the vertical cross sections and will be discussed in the following section.

Discussion

Evidence for the existence of melts in the crust beneath the ORZ

Low velocities are observed in the crystalline crust beneath the ORZ compared to the surrounding regions (5 and 25 km, Figs. 6a,b, and 7), as also revealed by a previous shear velocity model of the region (Fadel *et al.*, 2020). At 5 km depth (Fig. 6a), the observed low velocities within the rift from our model (~3.45 km/s) are slightly higher than those from the previous model (~3.35 km/s). This may be due to the fact that we independently set an upper layer for the low-velocity sediments in each initial model, so that velocities of structures deeper than the sediments are less influenced by the unconsolidated sediments. Low-velocity values within the rift from the two models become closer at a greater depth of 25 km (~3.65 km/s, Fig. 6b). The low velocities could be attributed to the melts or magma in the rifted crust as proposed previously (Leseane *et al.*, 2015; Fadel *et al.*, 2020). The high-crustal V_P/V_S values within the ORZ, reaching up to 1.91 (Yu, Liu, *et al.*, 2015; Wang *et al.*, 2025), are consistent with the inference of the presence of melts in the crust, with a melt fraction of ~10% (Feng *et al.*, 2023). Our velocity model shows that

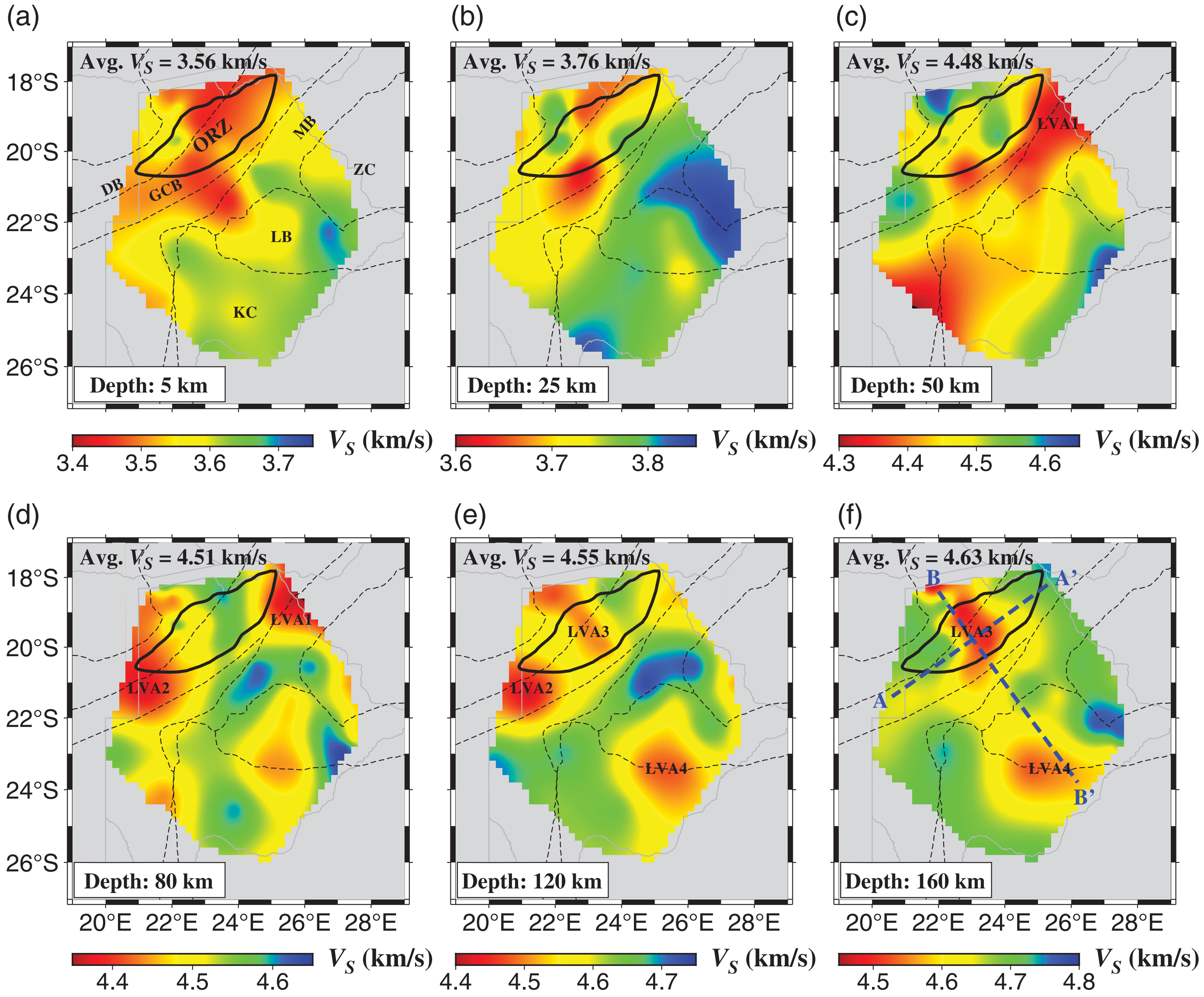

Figure 6. Horizontal shear-wave velocity slices at different depths. (a) 5, (b) 25, (c) 50, (d) 80, (e) 120, and (f) 160 km. Avg. V_S, average shear velocity; DB, Darama belt; GCB, Ghanzi–Chobe belt; KC, Kaapvaal craton; LB, Limpopo belt; MB, Magondi belt; ORZ, Okavango rift zone; and ZC, Zimbabwe craton.

at a depth of 25 km, the inverted shear-wave velocities beneath the ORZ can be as low as ~3.65 km/s (Fig. 6b), which is ~2.7% lower than the global averaged values of 3.75 km/s (Kennett and Engdahl, 1991), further supporting the presence of melts in the crust.

The melts could be generated in the crust through partial melting associated with continental extension during the rifting. Alternatively, they may be intruded from the underlying mantle, as observed beneath other continental rifts of the EARS (Ebinger and Sleep, 1998; Rychert *et al.*, 2012; Mulibo and Nyblade, 2013; Emry *et al.*, 2019) and elsewhere around the world (Coleman and McGuire, 1988; Baldridge *et al.*, 1991; Fu and Li, 2014; Grauch *et al.*, 2017). Previous investigations have proposed that the melts in the crust are intruded from a low-velocity anomaly in the upper mantle directly beneath the ORZ (Ortiz *et al.*, 2019; Yu *et al.*, 2017; Fadel *et al.*, 2020). Based on the shallow Curie depth and a 2D structural model from gravity data (Leseane *et al.*, 2015), the low-velocity anomaly in the upper mantle may indicate hot fluids or melts sourced from the asthenosphere (Leseane *et al.*, 2015; Fadel *et al.*, 2020). This anomaly is also identified in our velocity model starting from approximately 110 km deep (LVA3 in Figs. 6 and 7), which is generally consistent with other velocity models (~130 km deep, Fadel *et al.*, 2020; ~100 km deep, Yu *et al.*, 2017). It has been imaged that LVA3 extends to the mantle transition zone (~400 to 500 km deep, Ortiz *et al.*, 2019; Yu *et al.*, 2017), whereas our results could only exhibit the anomaly to ~160 km deep due to the limit of the depth of our model. In addition, we found three other low-velocity anomalies in the upper mantle, and some of them may also serve as potential melt reservoirs for intrusions into the rifted crust.

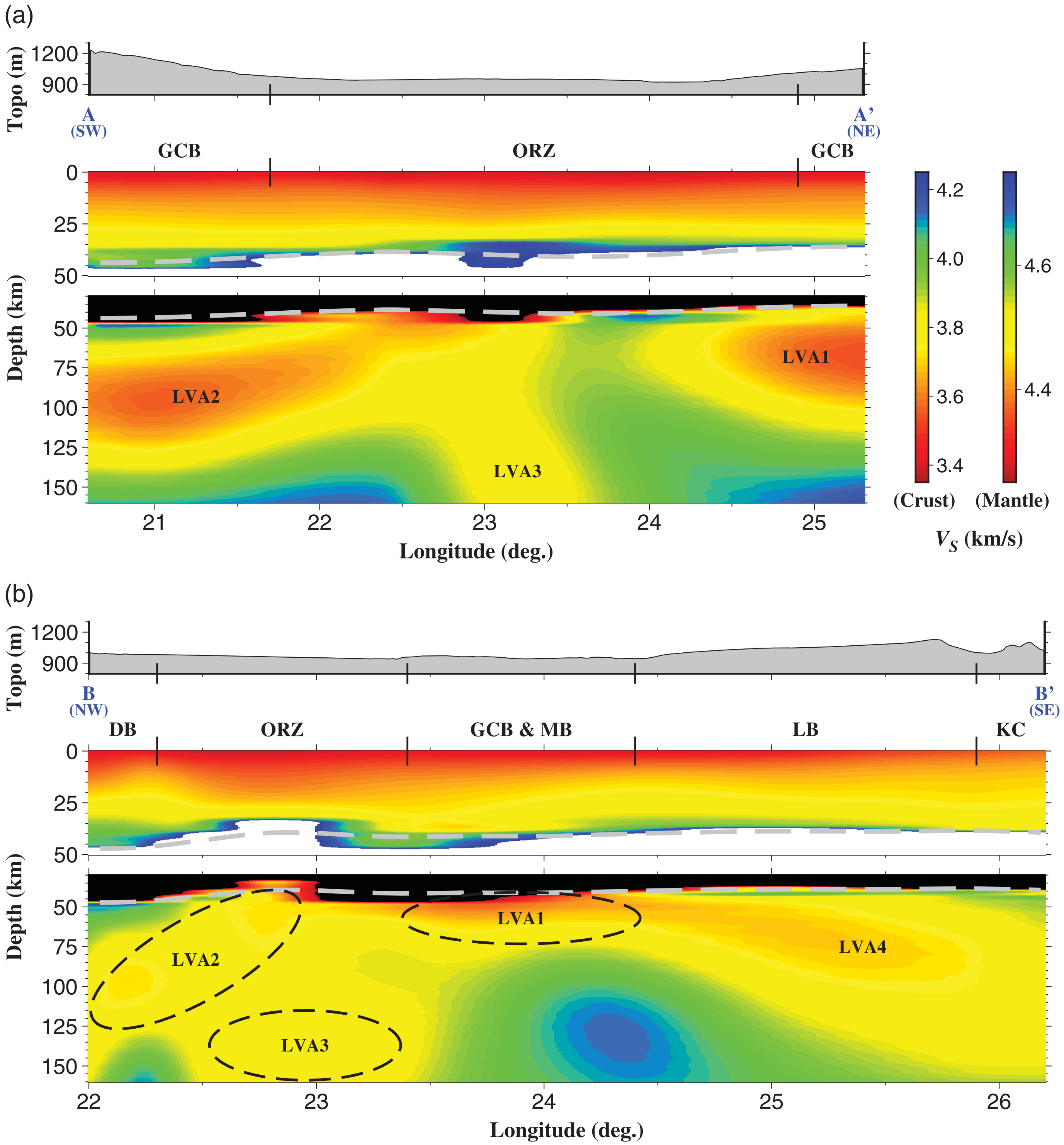

Figure 7. Vertical cross sections along the two profiles marked in Figure 6f. (a) Along profile AA′ paralleling to the rift axis. The upper panel is the elevation variation along the profile. The middle panel shows the shear velocity distribution from the surface to 50 km depth, with the gray dashed curve representing the Moho variation from a previous RF study (Wang *et al.*, 2025). The lower panel shows the shear velocity distribution from 30 to 160 km depth. (b) Similar to panel (a), but for profile BB′ transecting the rift. DB, Damara belt; GCB, Ghanzi–Chobe belt; KC, Kaapvaal craton; LB, Limpopo Belt; MB, Magondi belt; and ORZ, Okavango rift zone.

Two of the anomalies are located near the ends of the ORZ, within the surrounding orogenic belts (LVA1 and LVA2 in Figs. 6 and 7). The third one is situated in the boundary between the Limpopo belt and Kaapvaal craton (LVA4 in Figs. 6 and 7), likely caused by compositional refertilization associated with Precambrian magmatic events.

Characterizing low-velocity anomalies in the lithospheric mantle

The most distinct low-velocity anomalies observed in the lithospheric mantle are those around both ends of the ORZ (LVA1 and LVA2 in Figs. 6c,d, and 7). LVA1 is found in the Magondi and Ghanzi–Chobe belts near the northern end of the ORZ, whereas LVA2 is in the Damara and Ghanzi–Chobe belts near the southern end of the rift. These Paleoproterozoic–Early Paleozoic belts (Treloar, 1988; Schwartz *et al.*, 1996; Modie, 2000; Li *et al.*, 2008; Foster *et al.*, 2015), which are considered as pre-existing weak zones (Begg *et al.*, 2009), are currently undergoing extension associated with the rifting. Continental stretching facilitates lithospheric thinning (James *et al.*, 2001; Muller *et al.*, 2009; Khoza *et al.*, 2013; Yu *et al.*, 2017; Afonso *et al.*, 2022), which reduces the pressure and elevates the temperature in the lithosphere, creating an appropriate condition for the rocks to be molten (e.g., Rychert *et al.*, 2012; Feng *et al.*, 2023). The lithospheric stretching factor, a ratio between the stretched and initial lithospheric thickness (McKenzie, 1978; Chen, 2014), for these two low-velocity areas is ∼1.7 (Afonso *et al.*, 2022; Wang *et al.*, 2025), suggesting the occurrence of decompression melting (White and McKenzie, 1989). Our vertical profiles clearly exhibit that the mean shear velocities for the two anomalies are below 4.4 km/s at ∼100 km depth and diminish around 120 km (Fig. 7a), which suggests a high possibility of the presence of melts in the uppermost mantle (Hua *et al.*, 2023) and are hindered by the more rigid lithosphere at greater depths. The two anomalies are connected to the rifted crust (Fig. 7a) and appear to channel melts toward the rift axis (Fig. 8).

Another low-velocity anomaly in our model is the one located directly beneath the ORZ (LVA3 in Figs. 6e,f, and 7), which is consistent with the proposed regional thermal model (Leseane *et al.*, 2015) and body-wave-based velocity models of the upper mantle (Yu *et al.*, 2017; Ortiz *et al.*, 2019). Vertical profile BB′ suggests that LVA3 is constrained below ∼110 km depth and shows a weaker velocity reduction compared to LVA1 and LVA2 (Fig. 7). The mean shear-wave velocity value of LVA3 at 120 km depth is greater than 4.5 km/s (Figs. 6e and 7), suggesting either a quite small volume or even the absence of melts (Hua *et al.*, 2023). If a small volume of melts is present, since we observe little indication of low velocities in the uppermost mantle above LVA3 (50 and 80 km, Fig. 6c.d), the melts may migrate into the rifted crust through some narrow cracks (Fig. 8). Otherwise, LVA3 could also be associated with the elevated temperature of the region. The ORZ is characterized by a higher-than-normal heat flow value of ∼70 $\mathrm{mWm^{-2}}$ compared to the surrounding areas (Leseane *et al.*, 2015), possibly associated with the hot fluids at greater depths (Yu *et al.*, 2017; Ortiz *et al.*, 2019). Therefore, we postulate that LVA3 possibly represents either a small volume of melts feeding the rifted crust or a region with elevated temperatures or a combined result of both (Fig. 8).

We also notice that there's a low-velocity anomaly located beneath the boundary of the Limpopo belt and Kaapvaal craton, extending to at least 160 km depth (LVA4 in Figs. 6e,f, and 7b). The anomaly was previously identified by a continental-scale tomography investigation as well (Ortiz *et al.*, 2019). Although LVA4 seems to be connected with LVA1 feeding the rifted crust (Fig. 7b), the lower-than-normal heat flow value of less than 50 $\mathrm{mWm^{-2}}$ (Davies, 2013) and the absence of Phanerozoic tectonism in the region (Begg *et al.*, 2009) make it unlikely that the anomaly results from the presence of hot fluids or melts. The potential connection between LVA1 and LVA4 could be attributed to the limitation of model resolution. LVA4 may be attributed to compositional differences in the mantle, a common factor influencing seismic velocity anomalies. Our shear-wave velocity distribution in the upper mantle (120 and 160 km, Fig. 6e,f) is generally consistent with the compositional variation in the lithospheric mantle, in terms of the average Mg# ($\mathrm{Mg/(Mg + Fe^{2+})}$) (Afonso *et al.*, 2022). High Mg# values (>92) in the Zimbabwe and Kaapvaal cratons suggest a depleted lithospheric mantle, whereas low Mg# values (<91) in the Limpopo belt are indicative of refertilized compositions. This refertilized compositions may be associated with Precambrian magmatic events, such as the Bushveld (∼2.05 Ga) and/or Umkondo (∼1.1 Ga; Hoal, 2003; Fouch *et al.*, 2004; Ortiz *et al.*, 2019). It has been suggested that refertilized mantle materials can exhibit seismic velocity reductions of ∼1% (Jordan, 1979), since the proportion of the heavier Fe is elevated relatively (Tesauro *et al.*, 2014). Therefore, LVA4 may reflect the reduction of Mg# in the lithospheric mantle beneath the boundary of the Limpopo belt and Kaapvaal craton (Fig. 8).

Conclusions

We propose a 3D shear-wave velocity model beneath the incipient ORZ and adjacent regions. The velocity model, ranging from the surface to 160 km depth, is constructed using a nonlinear Bayesian Monte Carlo joint inversion of surface-wave dispersion and RFs analysis. Several structural features of the lithosphere are revealed by the new model. The observed velocity variations in both the crust and upper mantle suggest a certain degree of lithospheric deformation beneath the nascent rift zone. Within the rifted crust, the low velocities from our model support the previous inferences of the presence of melts. Our model also depicts four low-velocity anomalies in the lithospheric mantle. Two of them are located in the two

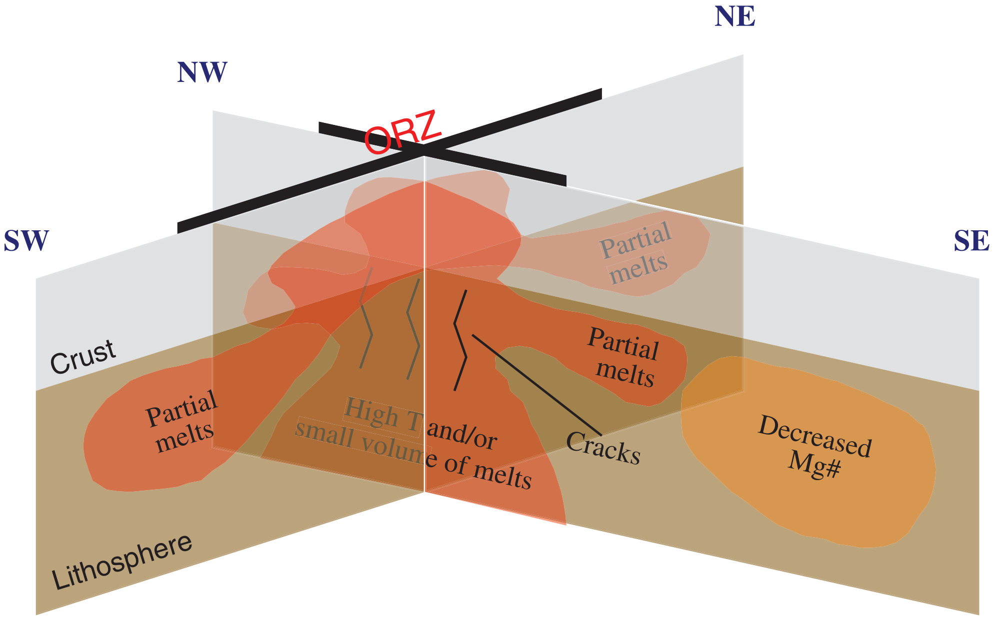

Figure 8. A conceptual sketch illustrating the lithospheric structure beneath the ORZ and adjacent regions. T, temperature.

corners of the rift, possibly reflecting decompression melting caused by the extension of the continent during rifting. Another one is identified directly beneath the rift with a much smaller velocity reduction. We speculate the anomaly might be a combined result of small volume of melts and higher-than-normal temperature in the lithosphere. These anomalies may serve as reservoirs providing melts or magma into the rifted crust. The last low-velocity anomaly is found beneath the boundary of the Limpopo belt and Kaapvaal craton, to the southeast of the rift. This anomaly may result from the refertilization of mantle rocks (reduction of Mg#) associated with the lithospheric modification by the Bushveld and Umkondo magmatic events, and thus would not supply the rifted crust with melts.

Data and Resources

The seismic data applied are archived at the Seismological Facility for the Advancement of Geosciences Data Management Center (SAGE-DMC) (https://ds.iris.edu/ds/nodes/dmc, last accessed May 2023). The seismic stations that provide data are from the following open networks: (a) the AF (Penn State University, 2004); (b) the XK (Gao *et al.*, 2012); and (c) the NR (Utrecht University [UU Netherlands], 1983); the BX (Botswana Geoscience Institute, 2001). The BREQ_FAST procedure (https://ds.iris.edu/ds/nodes/dmc/forms/breqfast-request, last accessed May 2023) is used for requesting all the seismic data. The Seismic Arrays for African Rift Initiation (SAFARI) is available at doi: 10.7914/SN/XK_2012. The Botswanan Network of Autonomously Recording Seismographs (BNARS) is available at doi: 10.7914/SN/NR. The Botswana Seismological Network (BSN) is available at doi: 10.7914/SN/BX. The AfricaArray network (AF) is available at doi: 10.7914/SN/AF. The supplemental material for this article includes (1) all the 27 stacked receiver functions (RFs) used for the joint inversion in this study (Fig. S1), (2) the selection of weighting factors for the joint inversion (Text S1 and Fig. S2), (3) the determination of the prior and posterior distribution (Text S2), (4) the selection of correlation length (Text S3 and Fig. S3), and (5) the Moho variation of the study region (Fig. S4).

Declaration of Competing Interests

The authors acknowledge that there are no conflicts of interest recorded.

Acknowledgments

The authors acknowledge the Seismological Facility for the Advancement of Geosciences Data Management Center (SAGE-DMC) for providing the waveforms and related metadata. SAGE Data Services are funded by the U.S. National Science Foundation (NSF) under Cooperative Support Agreement EAR-1851048. This research is jointly funded by the National Natural Science Foundation of China (Grant Number 42304059) to T. W., the National Natural Science Foundation of China (Grant Number 42288201) to L. C., and the National Natural Science Foundation of China (Grant Number 42374054) to Y. Y. Figures presented in this article were generated using the Generic Mapping Tools (GMT) software (Wessel *et al.*, 2019). The authors are grateful to Editor-in-Chief Allison Bent and two anonymous reviewers for their constructive comments, which have greatly improved the article.

References

Afonso, J. C., W. Ben-Mansour, S. Y. O'Reilly, W. L. Griffin, F. Salajegheh, S. Foley, G. Begg, K. Selway, A. Macdonald, N. Januszczak, *et al.* (2022). Thermochemical structure and evolution of cratonic lithosphere in central and southern Africa, *Nature Geosci.* **15,** no. 5, 405–410, doi: 10.1038/s41561-022-00929-y.

Ammon, C. J. (1991). The isolation of receiver effects from teleseismic *P* waveforms, *Bull. Seismol. Soc. Am.* **81,** no. 6, 2504–2510, doi: 10.1785/BSSA0810062504.

Baker, B., and J. Wohlenberg (1971). Structure and evolution of the Kenya Rift Valley, *Nature* **229,** no. 5286, 538–542, doi: 10.1038/229538a0.

Baldridge, W. S., Y. Eyal, Y. Bartov, G. Steinitz, and M. Eyal (1991). Miocene magmatism of Sinai related to the opening of the red sea, *Tectonophysics* **197,** nos. 2/4, 181–201, doi: 10.1016/0040-1951(91)90040-Y.

Begg, G. C., W. L. Griffin, L. M. Natapov, S. Y. O'Reilly, S. P. Grand, C. J. O'Neill, J. M. A. Hronsky, Y. P. Djomani, C. J. Swain, T. Deen, and P. Bowden (2009). The lithospheric architecture of Africa:

Seismic tomography, mantle petrology, and tectonic evolution, *Geosphere* **5,** no. 1, 23–50, doi: 10.1130/GES00179.S2.

Bensen, G. D., M. H. Ritzwoller, M. P. Barmin, A. L. Levshin, F. Lin, M. P. Moschetti, N. M. Shapiro, and Y. Yang (2007). Processing seismic ambient noise data to obtain reliable broad-band surface wave dispersion measurements, *Geophys. J. Int.* **169,** no. 3, 1239–1260, doi: 10.1111/j.1365-246x.2007.03374.x.

Bodin, T., M. Sambridge, H. Tkalcic, P. Arroucan, K. Gallagher, and N. Rawlinson (2012). Transdimensional inversion of receiver functions and surface wave dispersion, *J. Geophys. Res.* **117,** no. B2, doi: 10.1029/2011JB008560.

Bonini, M., G. Corti, F. Innocenti, P. Manetti, F. Mazzarini, T. Abebe, and Z. Pecskay (2005). Evolution of the Main Ethiopian Rift in the frame of Afar and Kenya rifts propagation, *Tectonics* **24,** no. 1, TC1007, doi: 10.1029/2004TC00168.

Boone, S. C., B. P. Kohn, A. J. W. Gleadow, C. K. Morley, C. Seiler, and D. A. Foster (2019). Birth of the East African Rift System: Nucleation of magmatism and strain in the Turkana Depression, *Geology* **47,** no. 9, 886–890, doi: 10.1130/G46468.1.

Botswana Geoscience Institute (2001). Botswana Seismological Network (BSN) [Data set], *International Federation of Digital Seismograph Networks*, doi: 10.7914/SN/BX.

Brocher, T. M. (2005). Empirical relations between elastic wavespeeds and density in the Earth's crust, *Bull. Seismol. Soc. Am.* **95,** no. 6, 2081–2092, doi: 10.1785/0120050077.

Brune, S., G. Corti, and G. Ranalli (2017). Controls of inherited lithospheric heterogeneity on rift linkage: Numerical and analog models of interaction between the Kenyan and Ethiopian rifts across the Turkana depression, *Tectonics* **36,** no. 9, 1767–1786, doi: 10.1002/2017tc004739.

Chen, L. (2014). Stretching factor estimation for the long-duration and multi-stage continental extensional tectonics: Application to the Baiyun Sag in the northern margin of the South China Sea, *Tectonophysics* **611,** no. 11, 167–180, doi: 10.1016/j.tecto.2013.11.026.

Chiasera, B., T. O. Rooney, I. D. Bastow, G. Yirgu, E. B. Grosfils, D. Ayalew, P. Mohr, J. Zimbelman, and M. Ramsey (2021). Magmatic rifting in the Main Ethiopian Rift began in thick continental lithosphere; the case of the Galema Range, *Lithos* **406–407,** 106494, doi: 10.1016/j.lithos.2021.106494.

Christensen, N. I., and W. D. Mooney (1995). Seismic velocity structure and composition of the continental crust: A global view, *J. Geophys. Res.* **100,** no. B6, 9761–9788, doi: 10.1029/95JB00259.

Coleman, R. G., and A. V. McGuire (1988). Magma systems related to the Red Sea opening, *Tectonophysics* **150,** nos. 1/2, 77–100, doi: 10.1016/0040-1951(88)90296-X.

Corti, G. (2009). Continental rift evolution: From rift initiation to incipient break-up in the Main Ethiopian Rift, East Africa, *Earth Sci. Rev.* **96,** no. 1, 1–53, doi: 10.1016/j.earscirev.2009.06.005.

Cunningham, E., and V. Lekic (2019). Constraining crustal structure in the presence of sediment: A multiple converted wave approach, *Geophys. J. Int.* **219,** no. 1, 313–327, doi: 10.1093/gji/ggz298.

Davies, J. H. (2013). Global map of solid Earth surface heat flow, *Geochem. Geophys. Geosys.* **14,** no. 10, 4608–4622, doi: 10.1002/ggge.20271.

Dugda, M. T., A. A. Nyblade, J. Julia, C. A. Langston, C. J. Ammon, and S. Simiyu (2005). Crustal structure in Ethiopia and Kenya from receiver function analysis: Implications for rift development in eastern Africa, *J. Geophys. Res.* **110,** no. B1, B01303, doi: 10.1029/2004JB003065.

Dziewonski, A., and D. Anderson (1981). Preliminary reference Earth model, *Phys. Earth Planet. In.* **25,** no. 4, 297–356, doi: 10.1016/0031-9201(81)90046-7.

Dziewonski, A. M., S. Bloch, and M. Landisman (1969). A technique for the analysis of transient seismic signals, *Bull. Seismol. Soc. Am.* **59,** no. 1, 427–444, doi: 10.1785/BSSA0590010427.

Ebinger, C. J., and N. H. Sleep (1998). Cenozoic magmatism throughout east Africa resulting from impact of a single plume, *Nature* **395,** no. 6704, 788–791, doi: 10.1038/27417.

Emry, E. L., Y. Shen, A. A. Nyblade, A. Flinders, and X. Bao (2019). Upper mantle Earth structure in Africa from full-wave ambient noise tomography, *Geochem. Geophys. Geosys.* **20,** no. 1, 120–147, doi: 10.1029/2018GC007804.

Fadel, I., H. Paulssen, M. van der Meijde, M. Kwadiba, O. Ntibinyane, A. Nyblade, and R. Durrheim (2020). Crustal and upper mantle shear wave velocity structure of Botswana: The 3 April 2017 central Botswana earthquake linked to the East African Rift System, *Geophys. Res. Lett.* **47,** no. 4, e2019GL085598, doi: 10.1029/2019GL085598.

Fadel, I., M. van der Meijde, and H. Paulssen (2018). Crustal structure and dynamics of Botswana, *J. Geophys. Res.* **123,** no. 12, 10,659–10,671, doi: 10.1029/2018JB016190.

Feng, M., S. Wei, L. Chen, U. Muksin, K. Lythgoe, T. Wang, and Z. Wu (2023). Pervasive crustal volcanic mush in the highly stretched Sunda Plate Margin of Northern Sumatran, *Geophys. Res. Lett.* **50,** no. 21, e2023GL104391, doi: 10.1029/2023GL104391.

Foster, D. A., B. D. Gosconbe, B. Newstead, B. Mapani, P. A. Mueller, L. C. Gregory, and E. Muvangua (2015). U-Pb age and Lu-Hf isotopic data of detrital zircons from the Neoproterozoic Damara Sequence: Implications for Congo and Kalahari before Gondwana, *Gondwana Res.* **28,** no. 1, 179–190, doi: 10.1016/j.gr.2014.04.011.

Fouch, M. J., D. E. James, J. C. VanDecar, S. van der Lee, and the Kaapvaal Seismic Group (2004). Mantle seismic structure beneath the Kaapvaal and Zimbabwe cratons, *S. Afr. J. Geol.* **107,** nos. 1/2, 33–44, doi: 10.2113/107.1-2.33.

Fu, Y., and A. Li (2014). Crustal shear wave velocity and radial anisotropy beneath the Rio Grande rift from ambient noise tomography, *J. Geophys. Res.* **120,** no. 2, 1005–1019, doi: 10.1002/2014JB011602.

Gao, S., K. Liu, M. Abdelsalam, and J. Hogan (2012). Seismic Arrays for African Rift Initiation (SAFARI) [Data set], *International Federation of Digital Seismograph Networks*, doi: 10.7914/SN/XK_2012.

Grauch, V. J. S., P. W. Bauer, B. J. Drenth, and K. I. Kelson (2017). A shifting rift-Geophysical insights into the evolution of Rio Grande rift margins and the Embudo transfer zone near Taos, New Mexico, *Geosphere* **16,** 870–910, doi: 10.1130/GES01425.1.

Hoal, K. O. (2003). Samples of Proterozoic iron-enriched mantle from the Premier kimberlite, *Lithos* **71,** nos. 2/4, 259–272, doi: 10.1016/S0024-4937(03)00116-6.

Hua, J., K. M. Fischer, T. W. Becker, E. Gazel, and G. Hirth (2023). Asthenospheric low-velocity zone consistent with globally prevalent partial melting, *Nature Geosci.* **5,** no. 6, 175–181, doi: 10.1038/s41561-022-01116-9.

Hubert, J., K. Whaler, and S. Fisseha (2018). The electrical structure of the central Main Ethiopian Rift as imaged by magnetotellurics: Implications for magma storage and pathways, *J. Geophys. Res.* **123,** nos. 3/4, 6019–6032, doi: 10.1029/2017JB015160.

James, D. E., M. J. Fouch, J. C. VanDecar, S. van der Lee, and , and the Kaapvaal Seismic Group (2001). Tectospheric structure beneath southern Africa, *Geophys. Res. Lett.* **28,** no. 13, 2485–2488, doi: 10.1029/2000GL012578.

Jia, Z., H. Wu, J. Peng, Q. Lu, W. Huang, C. Liu, F. Wang, Y. Liu, and M. He (2023). The deep origin of ground fissures in the Kenya Rift Valley, *Sci. Rep.* **13,** no. 1, 3672, doi: 10.1038/s41598-023-30918-z.

Jordan, T. H. (1979). Mineralogies, densities and seismic velocities of garnet lherzolites and their geophysical implications, in *The Mantle Sample: Inclusions in Kimberlites and Other Volcanics*, Proc. of the Second International Kimberlite Conference, F. R. Boyd and H. O. A. Meyer (Editors), American Geophysical Union, Washington, D. C., 1–14, doi: 10.1029/SP016p0001.

Julia, J., C. J. Ammon, R. B. Herrmann, and A. M. Correig (2000). Joint inversion of receiver function and surface wave dispersion observations, *Geophys. J. Int.* **143,** no. 1, 99–112, doi: 10.1046/j.1365-246x.2000.00217.x.

Kanamori, H., and D. Anderson (1977). Importance of physical dispersion in surface wave and free oscillation problems: Review, *Rev. Geophys.* **15,** no. 1, 105–112, doi: 10.1029/RG015i001p00105.

Karato, S. (1993). Importance of anelasticity in the interpretation of seismic tomography, *Geophys. Res. Lett.* **20,** no. 15, 1623–1626, doi: 10.1029/93GL01767.

Kennett, B. L. N., and E. R. Engdahl (1991). Traveltimes for global earthquake location and phase identification, *Geophys. J. Int.* **105,** no. 2, 429–465, doi: 10.1111/j.1365-246X.1991.tb06724.x.

Khoza, T. D., A. G. Jones, M. R. Muller, R. L. Evans, M. P. Miensopust, and S. J. Webb (2013). Lithospheric structure of an Archean craton and adjacent mobile belt revealed from 2-D and 3-D inversion of magnetotelluric data: Example from southern Congo craton in northern Namibia, *J. Geophys. Res.* **118,** no. 8, 4378–4397, doi: 10.1002/jgrb.50258.

Kinabo, B. D., J. P. Hogan, E. A. Atekwana, M. G. Abdelsalam, and M. P. Modisi (2008). Fault growth and propagation during incipient continental rifting: Insights from a combined aeromagnetic and Shuttle Radar Topography Mission digital elevation model investigation of the Okavango Rift Zone, northwest Botswana, *Tectonics* **30,** no. 3, 427–451, doi: 10.1029/2007TC002154.

Langston, C. A. (2011). Wave-field continuation and decomposition for passive seismic imaging under deep unconsolidated sediments, *Bull. Seismol. Soc. Am.* **101,** no. 5, 2176–2190, doi: 10.1785/0120100299.

Leseane, K., E. A. Atekwana, K. L. Mickus, M. G. Abdelsalam, E. M. Shemang, and E. A. Atekwana (2015). Thermal perturbations beneath the incipient Okavango Rift Zone, northwest Botswana, *J. Geophys. Res.* **120,** no. 2, 1210–1228, doi: 10.1002/2014JB011029.

Li, Z. X., S. V. Bogdanova, A. S. Collins, A. Davidson, B. De Waele, R. E. Ernst, I. C. W. Fitzsimons, R. A. Fuck, D. P. Gladkochub, J. Jacobs, *et al.* (2008). Assembly, configuration, and break-up history of Rodinia: A synthesis, *Precambr. Res.* **160,** nos. 1/2, 179–210, doi: 10.1016/j.precamres.2007.04.021.

Mackenzie, G. D., H. Thybo, and P. K. H. Maguire (2005). Crustal velocity structure across the Main Ethiopian Rift: Results from two-dimensional wide-angle seismic modelling, *Geophys. J. Int.* **162,** no. 3, 994–1006, doi: 10.1111/j.1365-246X.2005.02710.x.

Majaule, T., R. E. Hanson, R. M. Key, S. J. Singletary, M. W. Martin, and S. A. Bowring (2001). The Magondi belt in northeast Botswana: Regional relations and new geochronological data from the Sua Pan area, *J. Afr. Earth Sci.* **32,** no. 2, 257–267, doi: 10.1016/S0899-5362(01)90006-5.

McKenzie, D. (1978). Some remarks on the development of sedimentary basins, *Earth Planet. Sci. Lett.* **40,** no. 1, 25–32, doi: 10.1016/0012-821X(78)90071-7.

Mechie, J., G. R. Keller, C. Prodehl, M. A. Khan, and S. J. Gaciri (1997). A model for the structure, composition and evolution of the Kenya rift, *Tectonophysics* **278,** nos. 1/4, 95–119, doi: 10.1016/S0040-1951(97)00097-8.

Miensopust, M. P., A. G. Jones, M. R. Muller, X. Garcia, and R. L. Evans (2011). Lithospheric structures and Precambrian terrane boundaries in northeastern Botswana revealed through magnetotelluric profiling as part of the Southern African Magnetotelluric Experiment, *J. Geophys. Res.* **116,** no. B2, B02401, doi: 10.1029/2010JB007740.

Modie, B. N. (2000). Geology and mineralisation in the Meso- to Neoproterozoic Ghanzi-Chobe belt of northwest Botswana, *J. Afr. Earth Sci.* **30,** no. 3, 467–474, doi: 10.1016/S0899-5362(00)00032-4.

Montagner, J.-P. (1986). Regional three-dimensional structures using long period surface waves, *Ann. Geophys.* **4,** no. 3, 283–294.

Mulibo, G. D., and A. A. Nyblade (2013). The P and S wave velocity structure of the mantle beneath eastern Africa and the African superplume anomaly, *Geochem. Geophys. Geosys.* **14,** no. 8, 2696–2715, doi: 10.1002/ggge.20150.

Muller, M. R., A. G. Jones, R. L. Evans, H. S. Grutter, C. Hatton, X. Garcia, M. P. Hamilton, M. P. Miensopust, P. Cole, T. Ngwisanyi, and D. Hutchins (2009). Lithospheric structure, evolution and diamond prospectivity of the Rehoboth Terrane and western Kaapvaal Craton, southern Africa: Constraints from broadband magnetotellurics, *Lithos* **112,** 93–105, doi: 10.1016/j.lithos.2009.06.023.

Nair, S. K., S. S. Gao, K. H. Liu, and P. G. Silver (2006). Southern African crustal evolution and composition: Constraints from receiver function studies, *J. Geophys. Res.* **111,** no. 2, B02304, doi: 10.1029/2005JB003802.

Ogden, C. S., D. Keir, I. D. Bastow, A. Ayele, S. Marcou, F. Ugo, A. Woodward, B. A. Kibret, and S. Gudbrandsson (2021). Seismicity and crustal structure of the southern Main Ethiopian Rift: New evidence from Lake Abaya, *Geochem. Geophys. Geosys.* **22,** no. 8, e2021GC009831, doi: 10.1029/2021GC009831.

Ortiz, K., A. Nyblade, M. van der Meijde, H. Paulssen, M. Kwadiba, O. Ntibinyane, R. Durrheim, I. Fadel, and K. Homman (2019). Upper mantle P and S wave velocity structure of the Kalahari Craton and surrounding Proterozoic Terranes, southern Africa, *Geophys. Res. Lett.* **46,** no. 16, 9509–9518, doi: 10.1029/2019GL084053.

Penn State University (2004). AfricaArray (AF) [Data set], *International Federation of Digital Seismograph Networks*, doi: 10.7914/SN/AF.

Pretorius, D. A. (1984). The Kalahari Foreland, its marginal troughs and overthrust belts, and the regional structure of Botswana (Information circular 169), University of the Witwatersrand.

Reeves, C. (1972). Rifting in the Kalahari? *Nature* **237,** no. 5350, 95–96, doi: 10.1038/237095a0.

Ringrose, S., P. Huntsman-Mapila, A. B. Kampunzu, W. Downey, S. Coetzee, B. Vink, W. Matheson, and C. Vanderpost (2005). Sedimentological and geochemical evidence for palaeo-environmental change in the Makgadikgadi subbasin, in relation to the MOZ rift depression, Botswana, *Palaeogeogr. Palaeoclimatol. Palaeoecol.* **217,** nos. 3/4, 256–287, doi: 10.1016/j.palaeo.2004.11.024.

Rychert, C. A., J. O. S. Hammond, N. Harmon, J. M. Kendall, D. Keir, C. Ebinger, I. D. Bastow, A. Ayele, M. Belachew, and G. Stuart (2012). Volcanism in the Afar Rift sustained by decompression melting with minimal plume influence, *Nature Geosci.* **5,** no. 6, 406–409, doi: 10.1038/ngeo1455.

Sabra, K. G., P. Gerstoft, P. Roux, W. A. Kuperman, and M. C. Fehler (2005a). Extracting time-domain Greens function estimates from ambient seismic noise, *Geophys. Res. Lett.* **32,** no. 3, L03310, doi: 10.1029/2004GL021862.

Sabra, K. G., P. Gerstoft, P. Roux, W. A. Kuperman, and M. C. Fehler (2005b). Surface wave tomography from microseisms in Southern California, *Geophys. Res. Lett.* **32,** no. 14, L14311, doi: 10.1029/2005GL023155.

Schwartz, M. O., Y. Y. Kwok, D. W. Davis, and P. Akanyang (1996). Geology, geochronology and regional correlation of the Ghanzi Ridge, Botswana, *S. Afr. J. Geol.* **99,** no. 3, 245–250.

Shapiro, N. M., and M. H. Ritzwoller (2002). Monte-Carlo inversion for a global shear-velocity model of the crust and upper mantle, *Geophys. J. Int.* **151,** no. 1, 88–105, doi: 10.1046/j.1365-246X.2002.01742.x.

Shen, W., M. H. Ritzwoller, and V. Schulte-Pelkum (2013). A 3-D model of the crust and uppermost mantle beneath the Central and Western US by joint inversion of receiver functions and surface wave dispersion, *J. Geophys. Res.* **118,** no. 1, 262–276, doi: 10.1029/2012JB009602.

Shen, W., M. H. Ritzwoller, V. Schulte-Pelkum, and F.-C. Lin (2013). Joint inversion of surface wave dispersion and receiver functions: A Bayesian Monte-Carlo approach, *Geophys. J. Int.* **192,** no. 2, 807–836, doi: 10.1093/gji/ggs050.

Tesauro, M., M. K. Kaban, W. D. Mooney, and S. A. P. L. Cloetingh (2014). Density, temperature, and composition of the North American lithosphere—New insights from a joint analysis of seismic, gravity, and mineral physics data: 2. Thermal and compositional model of the upper mantle, *Geochem. Geophys. Geosys.* **15,** no. 12, 4808–4830, doi: 10.1002/2014GC005484.

Treloar, P. J. (1988). The geological evolution of the Magondi Mobile Belt, Zimbabwe, *Precambr. Res.* **38,** no. 1, 55–73, doi: 10.1016/0301-9268(88)90093-9.

Utrecht University (UU Netherlands) (1983). NARS [Data set], *International Federation of Digital Seismograph Networks*, doi: 10.7914/SN/NR.

Van Schijndel, V., D. H. Cornell, D. Frei, S. L. Simonsen, and M. J. Whitehousw (2014). Crustal evolution of the Rehoboth Province from Archaean to Mesoproterozoic times: Insights from the Rehoboth Basement Inlier, *Precambr. Res.* **240,** 22–36, doi: 10.1016/j.precamres.2013.10.014.

Wang, T., L. Chen, S. S. Gao, and K. H. Liu (2025). Deciphering a quantitative relationship between rifting and crustal melt fraction: Insights from the incipient Okavango Rift Zone, *Geophys. Res. Lett.* **52,** no. 12, e2024GL111814, doi: 10.1029/2024GL111814.

Wang, T., J. Feng, K. H. Liu, and S. S. Gao (2019). Crustal structure beneath the Malawi and Luangwa Rift Zones and adjacent areas from ambient noise tomography, *Gondwana Res.* **67,** 197–198, doi: 10.1016/j.gr.2018.10.018.

Wessel, P., J. F. Luis, L. Uieda, R. Scharroo, F. Wobbe, W. H. F. Smith, and D. Tian (2019). The generic mapping tools version 6, *Geochem. Geophys. Geosys.* **20,** no. 11, 5556–5564, doi: 10.1029/2019GC008515.

White, R., and D. McKenzie (1989). Magmatism at rift zones: The generation of volcanic continental margins and flood basalts, *J. Geophys. Res.* **94,** no. B6, 7685–7729, doi: 10.1029/JB094Ib06P07685.

Woldegabriel, G., J. L. Aronson, and R. C. Walter (1990). Geology, geochronology, and rift basin development in the central sector of the Main Ethiopian Rift, *Geol. Soc. Am. Bull.* **102,** no. 4, 439–458, doi: 10.1130/0016-7606(1990)102<0439:GGARBD>2.3.CO;2.

Wolfenden, E., C. Ebinger, G. Yirgu, A. Deino, and D. Ayalew (2004). Evolution of the northern Main Ethiopian Rift: Birth of a triple junction, *Earth Planet. Sci. Lett.* **224,** nos. 1/2, 213–228, doi: 10.1016/j.epsl.2004.04.022.

Yang, Y., Y. Zheng, J. Chen, S. Zhou, S. Celyan, E. Sandvol, F. Tilmann, K. Priestley, T. M. Hearn, J. F. Ni, *et al.* (2010). Rayleigh wave phase velocity maps of Tibet and the surrounding regions from ambient seismic noise tomography, *Geochem. Geophys. Geosys.* **11,** no. 8, Q08010, doi: 10.1029/2010GC003119.

Yao, H., R. D. van der Hilst, and M. V. de Hoop (2006). Surface-wave array tomography in SE Tibet from ambient seismic noise and two-station analysis - I. Phase velocity maps, *Geophys. J. Int.* **166,** no. 2, 732–744, doi: 10.1111/j.1365-246X.2006.03028.x.

Yao, H., R. D. van der Hilst, and J.-P. Montagner (2010). Heterogeneity and anisotropy of the lithosphere of SE Tibet from surface wave array tomography, *J. Geophys. Res.* **115,** no. B12, B12307, doi: 10.1029/2009JB007142.

Yao, H., G. Xu, L. Zhu, and X. Xiao (2005). Mantle structure from inter-station Rayleigh wave dispersion and its tectonic implication in western China and neighboring regions, *Phys. Earth Planet. In.* **148,** no. 1, 39–54, doi: 10.1016/j.pepi.2004.08.006.

Yu, Y., K. H. Liu, Z. Huang, D. Zhao, C. A. Reed, M. Moidaki, J. Lei, and S. S. Gao (2017). Mantle structure beneath the incipient Okavango rift zone in southern Africa, *Geosphere* **13,** no. 1, 102–111, doi: 10.1130/GES01331.1.

Yu, Y., K. H. Liu, C. A. Reed, M. Moidaki, K. Mickus, E. A. Atekwana, and S. S. Gao (2015). A joint receiver function and gravity study of crustal structure beneath the incipient Okavango Rift, Botswana, *Geophys. Res. Lett.* **42,** no. 20, 8398–8405, doi: 10.1002/2015GL065811.

Yu, Y., J. Song, K. H. Liu, and S. S. Gao (2015). Determining crustal structure beneath seismic stations overlying a low-velocity sedimentary layer using receiver functions, *J. Geophys. Res.* **120,** no. 5, 3208–3218, doi: 10.1002/2014JB011610.

Zhu, L., and H. Kanamori (2000). Moho depth variation in southern California from teleseismic receiver functions, *J. Geophys. Res.* **105,** no. B2, 2969–2980, doi: 10.1029/1999JB900322.

Manuscript received 14 August 2025
Published online 15 May 2026